Temporally focused wide-field two-photon microscopy: Paraxial to vectorial

Elijah Y. S. Yew,[1] Colin J. R. Sheppard,[2] and Peter T. C. So[1,3,*]

[1]*Singapore MIT Alliance for Research and Technology, 1 CREATE Way, #10-01 CREATE Tower, Singapore 138602, Singapore*

[2]*Department of Nanophysics, Istituto Italiano di Tecnologia, Via Morego, 30, 1613 Genova, Italy*

[3] *Department of Mechanical and Biological Engineering, Massachusetts Institute of Technology, Cambridge, MA02139, USA*

ptso@mit.edu

Abstract: Temporal focusing allows for optically sectioned wide-field microscopy. The optical sectioning arises because this method takes a pulsed input beam, stretches the pulses by diffracting off a grating, and focuses the stretched pulses such that only at the focal plane are the pulses re-compressed. This approach generates nonlinear optical processes at the focal plane and results in depth discrimination. Prior theoretical models of temporal focusing processes approximate the contributions of the different spectral components by their mean. This is valid for longer pulses that have narrower spectral bandwidth but results in a systematic deviation when broad spectrum, femtosecond pulses are used. Further, prior model takes the paraxial approximation but since these pulses are focused with high numerical aperture (NA) objectives, the effects of the vectorial nature of light should be considered. In this paper we present a paraxial and a vector theory of temporal focusing that takes into account the finite spread of the spectrum. Using paraxial theory we arrive at an analytical solution to the electric field at the focus for temporally focused wide-field two-photon (TF2p) microscopy as well as in the case of a spectrally chirped input beam. We find that using paraxial theory while accounting for the broad spectral spread gives results almost twice vector theory. Experiment results agree with predictions of the vector theory giving an axial full-width half maximum (FWHM) of $2.1\,\mu m$ and $1.8\,\mu m$ respectively as long as spectral spread is taken into account. Using our system parameters, the optical sectioning of the TF2p microscope is found to be $8\,\mu m$. The optical transfer function (OTF) of a TF2p microscope is also derived and is found to pass a significantly more limited band of axial frequencies than a point scanning two-photon (2p) microscope or a single photon (1p) confocal microscope.

OCIS codes: (170.0180) Microscopy; (180.2520) Fluorescence microscopy; (180.4315) Nonlinear microscopy; (180.6900) Three-dimensional microscopy; (190.7110) Ultrafast nonlinear optics.

References and links

1. D. Oron, E. Tal, and Y. Silberberg, "Scanningless depth-resolved microscopy," Opt. Express **13**(5), 1468–1476 (2005).
2. G. H. Zhu, J. van Howe, M. Durst, W. Zipfel, and C. Xu, "Simultaneous spatial and temporal focusing of femtosecond pulses," Opt. Express **13**(6), 2153–2159 (2005).
3. A. Vaziri and C. V. Shank, "Ultrafast widefield optical sectioning microscopy by multifocal temporal focusing," Opt. Express **18**(19), 19645–19655 (2010).
4. E. Tal, D. Oron, and Y. Silberberg, "Improved depth resolution in video-rate line-scanning multiphoton microscopy using temporal focusing," Opt. Lett. **30**(13), 1686–1688 (2005).

#183262 - $15.00 USD Received 14 Jan 2013; revised 24 Apr 2013; accepted 26 Apr 2013; published 17 May 2013

5. O. D. Therrien, B. Aubé, S. Pagès, P. D. Koninck, and D. Côté, "Wide-field multiphoton imaging of cellular dynamics in thick tissue by temporal focusing and patterned illumination," Biomed. Opt. Express **2**(3), 696–704 (2011).
6. E. Papagiakoumou, F. Anselmi, A. Bègue, V. de Sars, J. Glückstad, E. Y. Isacoff, and V. Emiliani, "Scanless two-photon excitation of channelrhodopsin-2," Nat. Methods **7**(10), 848–854 (2010).
7. D. Kim and P. T. C. So, "High-throughput three-dimensional lithographic microfabrication," Opt. Lett. **35**(10), 1602–1604 (2010).
8. Y.-C. Li, L.-C. Cheng, C.-Y. Chang, C.-H. Lien, P. J. Campagnola, and S.-J. Chen, "Fast multiphoton microfabrication of freeform polymer microstructures by spatiotemporal focusing and patterned excitation," Opt. Express **20**(17), 19030–19038 (2012).
9. D. N. Vitek, D. E. Adams, A. Johnson, P. S. Tsai, S. Backus, C. G. Durfee, D. Kleinfeld, and J. A. Squier, "Temporally focused femtosecond laser pulses for low numerical aperture micromachining through optically transparent materials," Opt. Express **18**(17), 18086–18094 (2010).
10. C. Froehly, B. Colombeau, and M. Vampouille, "II Shaping and Analysis of Picosecond Light Pulses," in *Progress in Optics*, E. Wolf, ed. (Elsevier, 1983), pp. 63–153.
11. O. E. Martinez, J. P. Gordon, and R. L. Fork, "Negative group-velocity dispersion using refraction," J. Opt. Soc. Am. A **1**(10), 1003–1006 (1984).
12. M. E. Durst, G. H. Zhu, and C. Xu, "Simultaneous spatial and temporal focusing for axial scanning," Opt. Express **14**(25), 12243–12254 (2006).
13. H. Suchowski, D. Oron, and Y. Silberberg, "Generation of a dark nonlinear focus by spatio-temporal coherent control," Opt. Commun. **264**(2), 482–487 (2006).
14. M. M. Wefers and K. A. Nelson, "Space-time profiles of shaped utrafast optical waveforms," IEEE J. Quantum Electron. **32**(1), 161–172 (1996).
15. M. B. Danailov and I. P. Christov, "Time-Space Shaping of Light-Pulses by Fourier Optical-Processing," J. Mod. Opt. **36**(6), 725–731 (1989).
16. O. E. Martinez, "Grating and Prism Compressors in the Case of Finite Beam Size," J. Opt. Soc. Am. B **3**(7), 929–934 (1986).
17. D. Oron and Y. Silberberg, "Harmonic generation with temporally focused ultrashort pulses," J. Opt. Soc. Am. B **22**(12), 2660–2663 (2005).
18. B. Richards and E. Wolf, "Electromagnetic Diffraction in Optical Systems. II. Structure of the Image Field in an Aplanatic System," Proc. R. Soc. Lond. A Math. Phys. Sci. **253**(1274), 358–379 (1959).
19. C. J. R. Sheppard and K. G. Larkin, "The three-dimensional transfer function and phase space mappings," Optik (Stuttg.) **112**(5), 189–192 (2001).
20. M. R. Arnison and C. J. R. Sheppard, "A 3D vectorial optical transfer function suitable for arbitrary pupil functions," Opt. Commun. **211**(1-6), 53–63 (2002).
21. S. Akturk, X. Gu, M. Kimmel, and R. Trebino, "Extremely simple single-prism ultrashort- pulse compressor," Opt. Express **14**(21), 10101–10108 (2006).
22. C. W. McCutchen, "Generalized Aperture and the Three-Dimensional Diffraction Image," J. Opt. Soc. Am. **54**(2), 240–242 (1964).

1. Introduction

Temporally focused wide-field two-photon (TF2p) microscopy was introduced by Oron and Silberberg [1] and also by Zhu and associates [2]. It has been successfully implemented to image biological samples [3, 4], cellular dynamics [5, 6], as well as for microfabrication [7–9]. TF2p microscopy is, in essence, simply a 4-*f* pulse shaper proposed by Froehly, Colombeau, and Vampouille [10] and Martinez, Gordon, and Fork [11] with the exception that there is no second grating to recombine the pulse. TF2p microscopy works because of the time-bandwidth product which states that the product of the pulse width and the spectral content is a constant. In a typical experimental setup (Fig. 1), an ultrafast pulse is incident upon a grating. This approach separates the pulse into its constituent wavelengths each diffracting at an angle governed by the grating equation. A focusing lens converts the wavelength dependent angular separation of the spectrum into a wavelength dependent positional offset at the back focal plane of the objective. The objective collimates and recombines the various spectral components only within the focus of the objective. It is clear that with the exception of the grating and the focus, the pulse width is broadened substantially everywhere in between as a result of the constancy of the time-bandwidth product. This reduces the photon flux everywhere between the grating and the focus. It is only at the focal plane where the spectral components of the pulse overlap and are recombined. As a result of this recombination, the time-bandwidth product dictates that the pulse width is once again minimum everywhere across the plane and photon flux is high enough for nonlinear optical processes to occur.

#183262 - $15.00 USD Received 14 Jan 2013; revised 24 Apr 2013; accepted 26 Apr 2013; published 17 May 2013

An interesting point of the similarities between a TF2p microscope and a 4-f pulse shaper is that both positive and negative dispersion may be achieved [11]. This property has been exploited in temporal focusing to shift the position of the focal plane along the z-axis effectively creating an axial scan through optical means [12, 13]. This is done by deliberately up-chirping or down-chirping the beam. The design of a temporal focusing microscope is such that it is a 'zero-dispersion' line and the focal plane will shift to compensate for the chirp of the input beam.

At present the analysis of TF2p microscopy has been restricted to a pulse that is relatively long [2, 12, 14, 15] in which the spectrum of the pulse is taken to be small such that $k \ll k_0$, where k is the wave number of the spectral components of the pulse while k_0 is the mean wave wavenumber. At the same time, the paraxial approximation assumes a pencil of rays and the sines of the angles involved are small and may be approximated to the angle itself. This is clearly not the case for ultrafast pulses and high NA objectives. We find that it is more important to maintain the assumption that $k \ll k_0$ whereas the diffracted angle can be assumed to be small. This is in contrast to previous literature [2, 12]. In this paper, we will present TF2p microscopy using the paraxial and vectorial approaches and compare the validity of both approaches through experiment. We will also present the 3D OTF of a TF2p microscopy obtained from numerical calculation and experiment that has not been previously considered in detail.

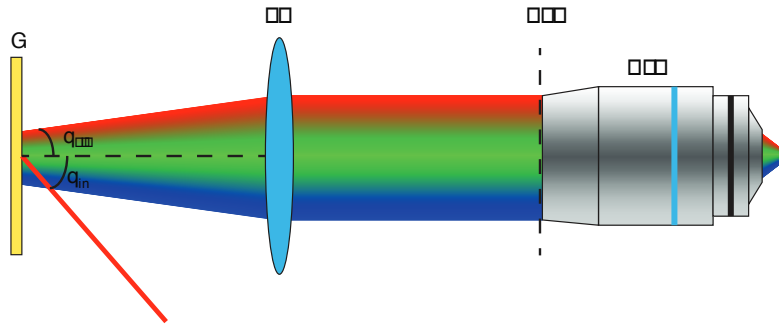

Fig. 1. The excitation beam is incident on the grating (G) at some angle θ_{in} such that the central wavelength λ_0 propagates along the optical axis after the grating. The grating disperses the spectrum of the pulse at some angle $\theta_{d,\lambda}$ which is dependent on the wavelength. The focusing tube lens (TL) focuses the spectrum at the back focal plane (BFP) of the objective (Obj). The function of the objective is to form an image of the grating in the object space. It is here that all the colors overlap thereby creating a plane of high photon flux necessary for nonlinear optical phenomenon.

2. Temporal focusing: Paraxial case

We define $\mathcal{F}^{(n)}[\cdot]$ as the n-th dimensional *spatial* Fourier transform and $\mathcal{F}[\cdot]$ as the *temporal* Fourier transform. For simplicity, we present the analysis in a single dimension (x) although we analyze it in both x and y. In a full 2D analysis, we find that the final result is similar except for a few higher order terms that are negligible.

We use the subscript G to denote the plane at the grating. For a beam incident on a grating, the electric field E_G just after the grating can be written as [16]:

$$E_G(x_G;\Delta k) = b_G \exp\left[ig_c \Delta k x_G - \frac{\gamma^2 x_G^2}{s_G^2}\right] \quad (1)$$

#183262 - $15.00 USD Received 14 Jan 2013; revised 24 Apr 2013; accepted 26 Apr 2013; published 17 May 2013

where b_G is some constant factor. For simplicity, the various variables in Eq. (1) has been tabulated in Table 1. We also assume space-time independence [14, 15].

Table 1. List of variables used

Variable name		Definition
c	=	Speed of light.
g	=	$2mp/\left(k_0 cd\cos q_{d,l}\right)$ where m is the diffraction order; d is the grating frequency; $k_0 = 2p/l_0$ is the wavenumber at the central wavelength l_0; and $q_{d,l}$ is the angle of diffraction and is dependent on the wavelength l.
k	=	$2p/l$, the wave number for which $k = Dk + k_0$ and $Dk = Dw/c$.
Dw	=	The shift of the angular frequency from the central (carrier) frequency w_0.
s_G	=	The size of the beam incident on the grating.
s_{BFP}	=	Size of the beam at the back focal plane of the objective and is given by $s_G = 4l_0 f_{TL}/\left(ps_0\right)$
q_{in}	=	The incidence angle of the beam on the grating.
y	=	$\cos q_{in}/\cos q_{d,l}$, and is a measure of the eccentricity of the beam cross-section due to diffraction.
$q_{d,l}$	=	$\sin^{-1}\left[2mp/\left\{d\left(\Delta k + k_0\right)\right\} - \sin q_{in}\right]$, and is the diffraction angle and is dependent on the wavelength.
t	=	The pulse width.
a	=	The chirp parameter.
f_{TL}	=	The focal length of the focusing tube lens.
f_O	=	The focal length of the objective.
M	=	f_{TL}/f_o, the magnification.
h	=	$\left\{e^{ikz}/\left(il z\right)\right\}\exp\left\{ik\left(x^2 + y^2\right)/\left(2z\right)\right\}$

In general, the ultrafast pulse from the laser can be expressed as

$$A\left(Dw\right) = \sqrt{\frac{t^2}{1 - ia}}\exp\left\{-\frac{it^2 Dw^2}{4\left(i + a\right)}\right\} \tag{2}$$

Here, t is the pulse width and a, the chirp parameter, indicates that the pulse has a linear frequency chirp (i.e. quadratic time dependent phase $f\left(t\right) = at^2/t^2$). For small values of a, the pulse width is nearly constant and will have an effect on the shifting of the focal plane which we will discuss later in this paper.

Following Fig. 1, the beam at the back focal plane (BFP) of the objective is focused by an achromatic doublet of focal length f_{TL}. In practice the f-number at this point is large and we may assume that the electric field in the BFP is adequately described using paraxial theory. For some particular wavenumber $k = Dk + k_0$ we may write the electric field (E_{BFP}) at the BFP of the objective as

#183262 - $15.00 USD Received 14 Jan 2013; revised 24 Apr 2013; accepted 26 Apr 2013; published 17 May 2013

$$E_{BFP}\left(x_{BFP};\Delta k\right) = A\left(\Delta\omega\right)\cdot E_G\left(x_G;\Delta k\right)$$
$$= b_{BFP}A\left(\Delta\omega\right)\exp\left[-\frac{\left(x_{BFP}-x_0\right)^2}{s_{BFP}^2}\right] \tag{3}$$

In this case $x_0 = f_{TL}g\Delta\omega/k$ simply represents the offset of the wavelength from the optical axis at the BFP and is related to the angle that light at some wavelength diffracts off the grating $\theta_{d,\lambda}$. The central wavelength λ_0 diffracts at an angle $\theta_{d,\lambda} = 0$. Since we assume paraxial rays, there is a direct relationship between the wavelength and the spatial offset at the BFP of the objective. From Eq. (3) we have s_{BFP} as being the radius of the focused spot at the BFP. We will first consider the paraxial case where the angles involved are small with the paraxial approximation and $\cos\theta_{d,\lambda} \approx 1$. With this approximation and the relation $M = f_o/f_{TL}$ the electric field at the focus of an objective of focal length f_o is just the Fourier transform of E_{BFP}. We differ from most previous literature [2, 12] as we have made the approximation of $\cos\theta_{d,\lambda} \approx 1$ but we do not make the assumption that $k \approx k_0$. Temporal focusing with a finite bandwidth in the paraxial approximation was treated by Oron and Silberberg [17] but we further extend their work by considering the effects of a chirped input beam. The resultant electric field $E_{TF,0}$ at the temporal focus is:

$$E_{TF,0}\left(x_{TF};\Delta k\right) = b_{TF}A\left(\Delta\omega\right)\exp\left[-\frac{y^2x_{TF}^2}{M^2s_G^2} - \frac{ic\Delta k g x_{TF}}{M}\right] \tag{4}$$

At some distance dz away from the focal plane, the electric field E_{TF} is given by convolving $E_{TF,0}$ with the free-space propagation kernel *h*. We can expand Eq. (4) to find that the chirp is compensated by a corresponding axial shift in the location of the focus as given in Eq. (5).

$$E_{TF}\left(dz,\Delta\omega\right) = b_{TF}\exp\left[-\frac{ig^2dz}{2k_0M^2 + \frac{8dz^2y^2}{k_0M^2s_G^4}}\Delta\omega^2 - \frac{it^2}{4\left(i+a\right)}\Delta\omega^2\right]$$
$$\cdot b_{TF}\exp\left[-\frac{ig^2dz}{2k_0M^2}\Delta\omega^2 - \frac{it^2}{4\left(i+a\right)}\Delta\omega^2\right] \tag{5}$$

Equation (5) tells us that for a given input chirp, the TF2p microscope shifts the temporal focus to compensate for the input chirp. This shift generates a group velocity dispersion (GVD) of equal magnitude ($ig^2dz/\left\{2k_0M^2\right\}$) and opposite sign to the chirp. E_{TF} is taken as a contribution over all *k* and is given by the temporal Fourier transform of Eq. (5) while Eq. (6) describes $I_{TF2p}\left(z\right)$. The latter equation is valid even with a 2D analysis and we have dropped negligible terms from the final answer. Given similar inputs but different system magnifications, the axial shift will vary by $1/M^2$. The extent of the shift (and the smallest amount of shift possible) is determined in part by the system magnification *M*. This may provide an extra degree of freedom or a constraint, especially since *M* is often fixed after taking into consideration factors such as the effective utilization of the NA.

#183262 - $15.00 USD Received 14 Jan 2013; revised 24 Apr 2013; accepted 26 Apr 2013; published 17 May 2013

$$I_{TF2p}(dz) = \left| \int\int E_{TF,0} \, h \right|^4 \cdot \frac{1}{1 + \frac{4ag^2}{M^2 k_0 t^2} dz + \frac{4(1+a^2)g^4}{M^4 k_0^2 t^4} dz^2} \cdot \frac{1}{1 + \left(a + \frac{G(1+a^2)}{M^2} dz \right)^2}. \quad (6)$$

For small values of chirp, $G = 2g^2 / (k_0 t^2)$ of Eq. (6) is a constant. The axial shift is linear for a given input chirp since $a^2 \neq 0$. At larger values of chirp, the shift becomes nonlinear through the term $(1+a^2)$, which is associated with *dz*. We note that in general, chirp broadens the pulse so G is no longer constant through t. For a transform limited pulse, this broadens the pulse. At the same time, the time-bandwidth product remains constant except that it is now scaled by the chirp parameter and is given by $\Delta\nu = 0.44\sqrt{1+a^2}/t_{FWHM}$. The TF2p setup compensates for this chirp by shifting the temporal focus to a position where the dispersion accumulated in the system negates the input chirp. Taking how the pulse broadens with chirp we can rewrite Eq. (6) as

$$I_{TF2p}(dz) \propto \frac{1}{1 + \left(a + c \frac{\Delta n^2}{M^2} dz \right)^2}. \quad (7)$$

In the paraxial limit, TF2p microscopy is therefore dependent on the frequency bandwidth and the system magnification as seen from Eq. (7) where $c = g^2 \log 2 / (0.22^2 k_0)$. The axial FWHM according to Eq. (7) is given by $2M^2/(c\Delta\nu^2)$ and is independent of the chirp. As we shall see later, this may come in useful as the paraxial approximation yields results that are close to a vector formulation.

3. Temporal focusing: Vectorial case

In general we use a high NA objective to improve the axial resolution at the focus. It is known that for values of NA above 0.5 the paraxial approximation is no longer valid and a vector theory of diffraction needs to be considered. We begin with a vectorized pupil as previously described [18]. In the focal plane the electric field can be written as

$$E(x,y,z) = \iint Q(x,h) \exp(ik\mathbf{q}\cdot\mathbf{r}) \frac{dx\,dh}{V}, \quad (8)$$

with $\mathbf{r} = x\mathbf{i} + y\mathbf{j} + z\mathbf{k}$ at the focus and $\mathbf{q} = x\mathbf{i} + h\mathbf{j} + V\mathbf{k}$ in the pupil. We recognize $Q(x,h)/V$ as the pupil function

$$P(x,h) = \frac{Q(x,h)}{V}. \quad (9)$$

For incident light that is linearly polarized, we can describe a strength function [19, 20] that is given by

#183262 - $15.00 USD Received 14 Jan 2013; revised 24 Apr 2013; accepted 26 Apr 2013; published 17 May 2013

$$a(x,h,V) = \begin{cases} \left(x^2 V + h^2\right)/l^2 \\ -xh\left(1-V\right)/l^2 \\ -x \end{cases} \tag{10}$$

where $l = \sqrt{x^2 + h^2}$ and $V = \sqrt{1-l^2}$. With this we can express the projected pupil function (in Cartesian coordinates) as

$$P(x,h) = a(x,h)\,S(x,h)\,\Phi(x,h), \tag{11}$$

where $S(x,h)$ is the apodization function and for lenses designed to meet the sine condition it is $\sqrt{\cos\theta}$ and for the Herschel condition it is 1. The function $\Phi(x,h)$ accounts for arbitrary transmission factors such as aberrations or a mask.

The electric field at the focus is taken over the limits of the pupil and is given by Eq. (8). We find the electric field at the BFP of the objective from Eq. (3) and for our vector formulation it is

$$\begin{aligned} E_{BFP}\left(x_{BFP}, y_{BFP}, z_{BFP}; \Delta k\right) &= A(\Delta k)\,\bar{\Omega}^{(2)} \left\{ \exp\left(ig\Delta w x\right) \exp\left[-\frac{y_{BFP}^2 + y^2 x_{BFP}^2}{s_G^2} \right] \right\} \\ &= A(\Delta k) \exp\left[-\frac{y^2 y_{BFP}^2 + \left(x_{BFP} - x_0\right)^2}{s_{BFP}^2} \right] \end{aligned} \tag{12}$$

and the variables have the same meaning as in Eq. (3) except for x_0, which is given by

$$x_0 = \frac{2m\pi f_{TL}\Delta k}{\left(\Delta k + k_0\right) d \sqrt{1 - \left[\frac{2m\pi}{d\left(\Delta k + k_0\right)} - \sin\theta_{in} \right]^2}}. \tag{13}$$

From Eq. (5) we can express the electric field at some point near the focus in terms of the projected vectorial pupil multiplied by a defocus term $\exp[ikz\cos\theta]$.

$$E_{TF,0}\left(x,y,z,\Delta k; z\right) = \bar{\Omega}^{(2)} \left\{ P\left(x,h,V,\Delta k\right) \exp\left[ik_z z - \frac{i\tau^2 c^2 \Delta k^2}{4\left(i+a\right)} \right] \right\} \tag{14}$$

Equation (14) is easy to evaluate with FFT algorithms and lends itself to sequential processing. The time varying electric field is therefore the temporal Fourier transform of Eq. (14).

$$\begin{aligned} E_{TF}\left(x,y,z,t\right) &= \int_{-\Delta k}^{\Delta k} E_{TF,0}\left(x,y,\Delta k; z\right) \exp\left(ick_0 t\right) d\left(\Delta k\right) \\ &= \Im\left\{ E_{TF,0}\left(x,y,\Delta k; z\right) \right\} \end{aligned} \tag{15}$$

The instantaneous intensity is thus $I = E \cdot E^*$ and for two-photon excitation it is the square of the intensity $I_{TF2p} = I^2$.

4. Optical transfer function (OTF)

The optical transfer function is a useful way of characterizing the performance of a microscope. In general we can express the OTF of an imaging system with a point detector as

#183262 - $15.00 USD Received 14 Jan 2013; revised 24 Apr 2013; accepted 26 Apr 2013; published 17 May 2013

$C(m,n,s) = \bar{F}^{(3)}\left(|h_{ex}|^{p}\,|h_{\mathrm{det}}|^{2}\right)$ where $p = 2$ for single photon and $p = 4$ for a two-photon microscope. A measure of the optical sectioning capability of a microscope is given by the response to an infinitely thin layer of fluorescence being scanned through the axis. As an alternative a thick layer of fluorescence may be scanned through the focus and the derivative of the axial response is a measure of the optical sectioning capability. This optical sectioning capability may be found from the OTF by taking the projection of the 3D OTF along s to give the integrated intensity. This may be expressed as

$$I_{TF2p}(z) = \int_{-\infty}^{\infty} C(0,0,s)\exp(izs)\,ds. \tag{16}$$

5. Results

A typical setup of a TF2p microscope is illustrated in Fig. 1. We used a Chameleon Ti:Sapphire (Coherent) operating at 790 nm. The repetition rate is 80 MHz and the output pulse was measured at 158 fs. The grating (Richardson Gratings) has a period of 600 lines/mm and the focusing tube lens is a 250 mm doublet. The Fluar 40x NA 1.3 Oil was used in all figures. In order to fully utilize the NA of the objective, we included a 2:1 beam expander (not shown in Fig. 1) after the grating and before the focusing tube lens. Fluorescent beads of 0.2 μm diameter (Polysciences) were used to measure the axial resolution. A dilute solution (1:500 v/v) of beads was dried on a coverslip and the coverslip attached to a glass slide.

A drop of Rhodamine B was diluted in water and 0.4 μL was placed on a clean coverslip and spread evenly over the surface to give a thin film of fluorescence that is 0.8 μm thick on average. The fluorescent beads and thin film of fluorescence were fixed to glass slides. A special holder was made to mount the slides onto a nano-positioning stage (nanoMIPOS400, Piezosystem Jena). This stage allowed repeatable movements of 100 nm resolution. For all experiments the fluorescence signal was captured in epi-fluorescence mode and imaged with a Zeiss tube lens and captured on a CCD (GE680, Allied Vision). The data was stored on a PC for post-processing with Matlab.

Figure 2 illustrates the difference between the FWHM of $I_{TF2p}(z)$ as calculated from paraxial and vectorial theory. It is clear that the paraxial form and vector theory give similar results, although the drop-off is slower for the vector theory. Paraxial theory gives a larger axial FWHM of 15.6 μm compared to 7.6 μm from vector theory. This is attributable to the fact that in the vector theory we account for factors such as the high NA, apodization, and that the wavefront after the objective is spherical and not parabolic. We note that up to the back focal plane of the objective, paraxial optics may be used since even for 100 fs pulses the angle of diffraction at the $1/e^2$ wavelength is small enough such that $\cos\theta_d \approx 1$. We choose to use the vector form in the rest of our paper as the computation time and resources is not significant and more importantly, it better approximates the data obtained.

We now consider the OTF of a TF2p microscope. The optical transfer function is an important concept because, as a single measure, it tells us much more about the performance of the microscope than other measures combined. Figure 3 shows the cross-sections of the 3D OTF i.e $C(0,n,s)$ of the 1p wide-field microscope, the 1p confocal microscope with a point detector, the 2p microscope, and the TF2p microscope. In Fig. 3(a), it is observed that the 1p wide-field microscope has a missing cone which means that it does not transmit any axial frequencies and the optical sectioning effect is non-existent. In Figs. 3(b) to 3(c), we find that the inclusion of a confocal pinhole or the use of 2p excitation results in optical sectioning. The OTF for a temporally focused wide-field 2p microscope is thus a mix between a wide-field and a 2p microscope. The transverse frequency support is similar to that of a 2p microscope. This missing cone is not truly missing as shown in Fig. 4.

#183262 - $15.00 USD Received 14 Jan 2013; revised 24 Apr 2013; accepted 26 Apr 2013; published 17 May 2013

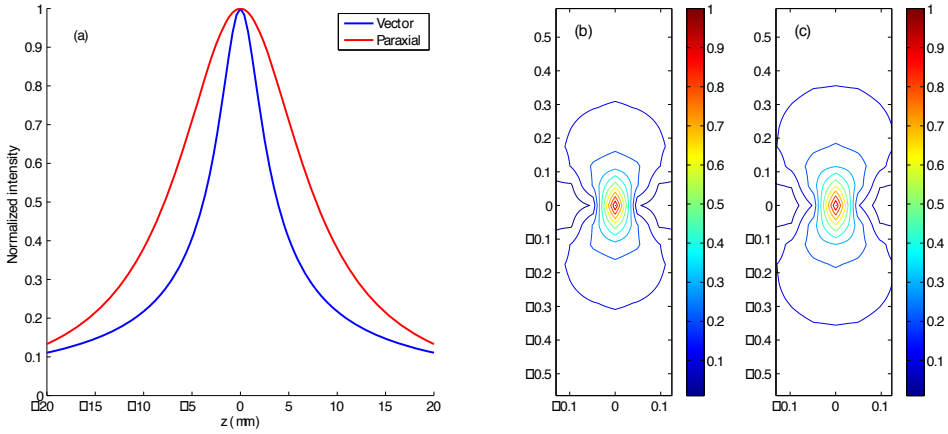

Fig. 2. (a) The envelope of the temporal focus *i.e* $I_{TF2p}(z)$ for the paraxial approximation (open blue circles) and that calculated from vector theory (red line). The FWHM for the paraxial approach is 15.6 μm whereas for the vector approach is 7.6 μm. (b) and (c) are the contour plots of the neck region of the OTF for paraxial and vector cases respectively.

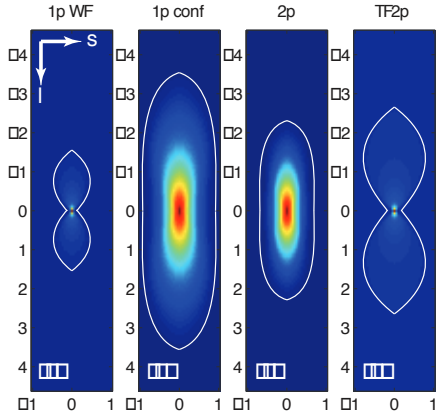

Fig. 3. (a) Slice view of the OTF for a 1p fluorescence wide-field microscope. The missing cone indicates that no axial information is transmitted. On the other hand, (b) is the slice of the 1p confocal microscope. The missing cone has been filled in and has optical sectioning. A similar OTF is found for (c) a conventional 2p microscope. (d) is the slice OTF of a TF2p microscope. The approximate extent of the OTF has been outlined in white as a visual aid.

Figure 4 shows a graph concerning $C(0,0,s)$ from the 3D OTF. The axial frequency support for a 2p microscope is given by $n(1-\cos\alpha)$. Given that the point spread function of a TF2p microscope has a FWHM of 1.8 μm, which is about twice that of a conventional 2p microscope at 0.8 μm, we expect the support for a TF2p microscope to be close to half that of the conventional 2p transfer function in the axial direction. Indeed Fig. 4 shows that the frequency supports for both microscopes are close to the values given above. Another interesting observation is that the drop-off is much quicker for a TF2p microscope.

This means that we lose axial information much quicker than compared to conventional 2p or 1p confocal microscopes. The axial resolution is therefore much poorer for a TF2p microscope. While this may be disadvantageous to some extent, this loss of resolution relative to 2p or 1p confocal microscopes may be overcome by the use of structured illumination methods.

#183262 - $15.00 USD Received 14 Jan 2013; revised 24 Apr 2013; accepted 26 Apr 2013; published 17 May 2013

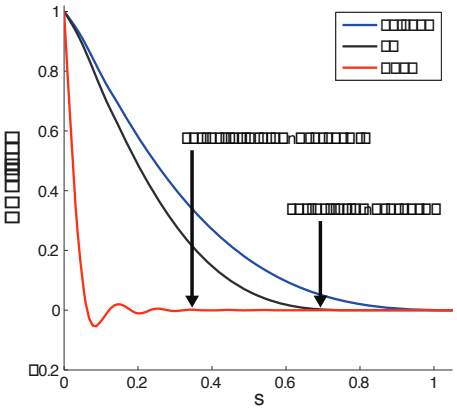

Fig. 4. Plotting the transfer function along the *s*-axis indicates that the frequency support for TF2p is close to half that of the conventional 2p transfer function. The 1p confocal has a frequency support twice that of conventional 2p. The cut-off frequency for the 2p microscope is about twice as large as that of a TF2p microscope. In all cases, the excitation wavelength was 790 nm and the emission wavelength of 395 nm.

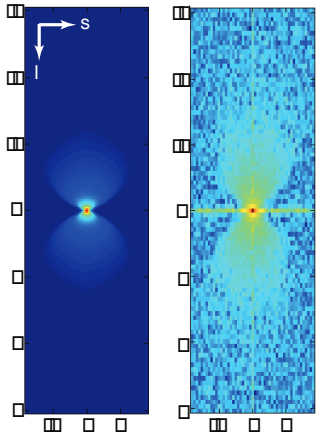

Fig. 5. Comparison between the numerically calculated OTF and that obtained experimentally. (a) The cross-section of the numerically calculated OTF and (b) experimentally obtained OTF. In both cases, the excitation wavelength was 790 nm and the emission wavelength was taken as 485 nm for (a).

We next compared the validity of our high aperture formulation of TF2p microscopy to that obtained experimentally. We obtained the 3D OTF by taking the 3D Fourier transform of the image of a single bead and Fig. 5 shows the cross-section through the numerically calculated and experimentally recorded OTF. Since the beads have a peak emission of fluorescence at 485 nm we normalized the spatial frequencies by 485 nm for both cases. It is clear that the theoretically derived OTF is validated by experiment. In both cases we find the same figure-of-eight shape and similar frequency support in both the *l* and the *s* directions.

A two-photon microscope is worth the complexity and expense because it is able to deliver optically sectioned images among other things. A TF2p microscope is able to provide the necessary spatial confinement for the two-photon process but the optical sectioning effect is poorer than that of a 1p confocal or a 2p microscope. We imaged a 0.2 μm fluorescent bead. We summed the image over a region equivalent to 2 Airy Units (A.U) and find that the FWHM of the imaged bead is 2.1 μm compared to 1.8 μm from theory while Fig. 6 shows the fit.

#183262 - $15.00 USD Received 14 Jan 2013; revised 24 Apr 2013; accepted 26 Apr 2013; published 17 May 2013

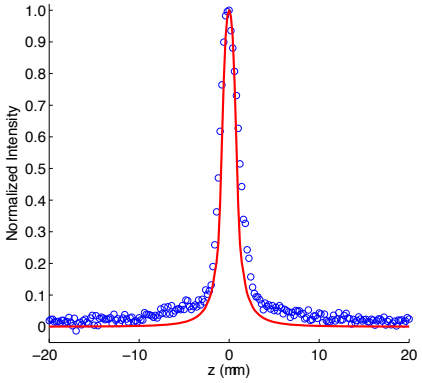

Fig. 6. Axial intensity of the image of a bead. Excitation and imaging was done with the same objective, a Zeiss 40x NA 1.3 oil immersion objective. The experiment (blue open circles) yielded a FWHM of 2.1 μm whereas numerical calculations (red solid line) gave a FWHM of 1.8 μm.

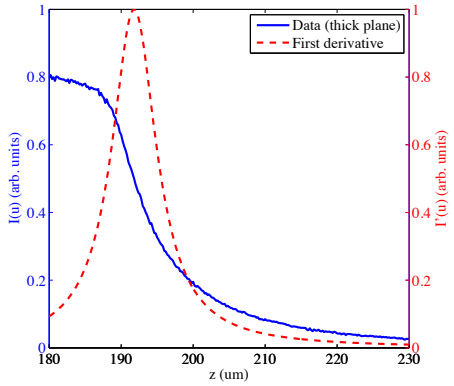

Fig. 7. A thick layer of Rhodamine was scanned through the temporal focus and the recorded signal (blue, solid line) is plotted. The first derivative of the signal was obtained and a curve fitted to it (red, dashed line). Both are measures of the optical sectioning property of the TF2p microscope.

Although the image of a single fluorescent bead provides a good estimate of the imaging properties of a microscope, a more common scenario found in imaging is to discriminate between signal that emanates from the in-focus plane and out-of-focus planes. For this purpose, the optical sectioning has been defined to be the response of the microscope to a plane of fluorescence with no transverse variations. Alternatively, it is the steepness of the gradient of the response due to a sea of fluorescence scanned through the focus. The signal of such an experiment was recorded and graphed in Fig. 7. The first derivative of the recorded signal, a measure of the optical sectioning capability of a microscope, was obtained and is also presented in the same figure. From the data, we find that the FWHM of the optical response to a sea of fluorescence (given by the dotted red curve) to be 7.6 μm. What this means is that we are only able to locate the interface of an axially extended object with no axial variation to within 7.6 μm.

We compared the optical response to a sea of fluorescence by measuring the optical sectioning effect, which is obtained by scanning a thin film of fluorescence through the focus. Figure 8 illustrates the response of the TF2p microscope due to a thin layer of fluorescence. The measured response has a FWHM of 8 μm and is in good agreement with the derived optical sectioning response from a sea of fluorescence as well as the response calculated

#183262 - $15.00 USD Received 14 Jan 2013; revised 24 Apr 2013; accepted 26 Apr 2013; published 17 May 2013

numerically. At this point, we note that the image of a thin plane of fluorescence (Fig. 8) is poorer than that of a sub-resolution bead because the former has mostly the DC term (zero frequency) in the Fourier space whereas the latter, being effectively a point, possesses higher spatial frequencies. This being the case, the effect of the OTF is such that the non-DC frequencies attenuate with defocus for the image of a bead whereas the DC term is always present and does not attenuate with defocus for the image of a thin plane.

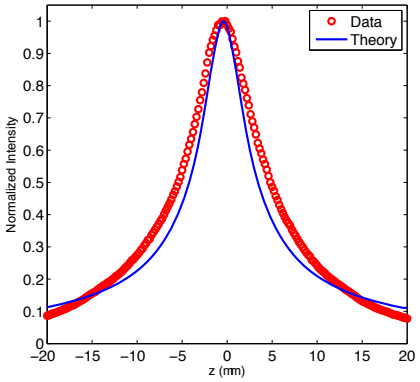

Fig. 8. A thin layer of fluorescence (red open circles) was scanned through the temporal focus and the captured image was summed over an area corresponding to around 2 Airy Units (AU). This experiment is equivalent to taking the first derivative of the optical response to a sea of fluorescence. The data is compared to vector theory (blue line) and a good fit is obtained between experiment and theory.

It has been demonstrated [12, 13] that the plane can be scanned along the optical axis simply through the introduction of a chirp to the excitation beam. Since paraxial theory indicates dependence upon $1/M^2$ (see Eq. (7)), we set up an experiment to test the validity of this dependence under conditions of high NA.

Table 2. Shift of temporal focus with chirp

Nos.	**Measured Pulsewidth (fs)**	**M_1 = 37.89 (1) z shift (µm)**	**M_2 = 60.61 (2) z shift (µm)**	**$(M_1/M_2)^2$ = 2.56 (1)/(2)**
A	169.4	3.39	1.34	2.53
B	181.3	3.47	1.35	2.57
C	244.6	3.5	1.45	2.41
D	326.6	3.57	1.32	2.70
E	404.3	3.71	1.15	3.22
F	497.2	3.62	1.43	2.53
G	706.3	3.69	1.37	2.69
H	851.9	3.62	1.54	2.35
	Mean	3.57	1.37	2.63

Columns 2 and 3 represents the shift of the temporal focusing plane, relative to the previous position attained.

We introduced a prism-based compensator [21] before the grating to vary the chirp of the input beam. The amount of chirp imparted to the beam was accomplished through translating the retroreflector as described in the reference [21]. A separate line fed the beam to an autocorrelator for measuring the pulsewidth. For each position of the retroreflector, we scanned a thin layer of Rhodamine 6G axially through the temporal focus and recorded the fluorescence signal with a CCD. This was repeated for two objectives, a Zeiss 25x NA 0.8 and a Zeiss 40x NA 1.3 Oil. The system magnification for both objectives is 37.89 and 60.61 respectively. Based on the recorded fluorescence signal for each scan, we fitted a Lorentzian function to the data and, by determining the axial position where a maximum signal was recorded, determined the axial position of the temporal focusing plane with position of the retroreflector (i.e chirp). We subsequently found the amount of shift that occurred between

#183262 - $15.00 USD Received 14 Jan 2013; revised 24 Apr 2013; accepted 26 Apr 2013; published 17 May 2013

each shifted plane. This was repeated for the various magnifications and entered in columns 2 and 3 in Table 2. From Table 2 the average shift in z between planes for the 25x objective is 3.57 μm. The 40x objective results in a system magnification that is 1.6 times larger than with the 25x objective. The change in the axial shift between planes is thus expected to be $3.57/1.6^2 = 1.39\,\mu\text{m}$. Indeed we find that the experimental shift of 1.37 μm agrees well with the expected result from our derivation. We can conclude that even in a high NA vector approach, the relative axial shift is still well approximated by the paraxial form where it was derived to be proportional to $1/M^2$.

6. Conclusion

We have analyzed temporal focusing using paraxial and vector theory. For the paraxial theory, we find that even for 100 fs pulses, we are justified in making the approximation $\cos\theta_{d,l} \approx 1$. On the other hand, keeping $k = \Delta k + k_0$ in the paraxial approximation still allows us to analyze temporal focusing using Fourier optics and derive an analytical solution for $I_{TF2p}(z)$. The analytic solution of the paraxial approximation gives an axial FWHM almost twice that of the vector case. The vector case was found to fit experiment better and, by recasting the problem as a projected pupil function, we were able to apply standard FFT algorithms and the chirp z-transform to minimize the computational process. Given our system parameters, we found a close fit between the numerical calculations and data obtained from experiment.

We also examined the 3D OTF of the TF2p microscope. We found that it is similar to the conventional wide-field microscope, the exception being that the missing cone is not exactly 'missing' but is slightly filled in as a result of the confinement due to the two-photon effect arising from temporal focusing. The frequency support for a TF2p microscope is half that of a conventional 2p microscope and this is reflected in the FWHM of the point spread function being almost twice that of a conventional 2p microscope. The transfer function for a TF2p also drops off much quicker than those of a conventional 2p or 1p confocal microscopes. The transverse frequency support is expanded and is similar to that of a 2p microscope. It is also interesting to consider the alternative, which is to consider the 3D pupil function [19, 22] to generate the 3D OTF of a temporally focused wide-field 2p microscope through the autocorrelation of the 3D pupil function.

Finally we examined how application of chirp to the input beam affects the axial shift of the temporal focus. Based on paraxial theory, we found that this shift is inversely proportional to the square of the system magnification. Our experiments show that the scaling factor predicted with paraxial theory is applicable even for high NA objectives. Since the utilization of the NA– which is to say the filling the BFP with the spectral bandwidth– is important for good axial resolution, the fixed bandwidth of the source and the finite size of the BFP often eventually dictates the overall system magnification. This has implications for the final field-of-view as well as the amount of axial scanning available.

The long tail of temporal focusing has an effect on the optical sectioning of the TF2p microscope. This may affect the imaging quality when the sample is highly scattering or the fluorophores are not sparsely distributed through the sample. It is conceivable that the TF2p microscope can also benefit from other background suppressing measures such as structured illumination. The extended drop-off will also have implications for microfabrication processes that rely on temporal focusing.

Acknowledgments

This research was supported by the National Research Foundation Singapore through the Singapore MIT Alliance for Research and Technology's BioSym research programme. PTCSO further acknowledges support from: NIH 9P41EB015871-26A1, R01-EX017656, 5 R01 NS051320, 4R44EB012415-02, NSF CBET-0939511, the Singapore-MIT Alliance 2, and the MIT SkolTech initiative.